

Quantifying the role of different surface coatings in experimental models of wound healing

Wang Jin ^{a,b,*}, Kai-Yin Lo ^c, Yung-Shin Sun ^d, Ya-Han Ting ^c,
Matthew J Simpson ^a,

^a*School of Mathematical Sciences, Queensland University of Technology (QUT),
Brisbane, Queensland 4000, Australia.*

^b*ARC Centre of Excellence for Mathematical and Statistical Frontiers, QUT,
Brisbane, Queensland 4000, Australia.*

^c*Department of Agricultural Chemistry, National Taiwan University,
Taipei 10617, Taiwan.*

^d*Department of Physics, Fu-Jen Catholic University, Taipei 242, Taiwan.*

Abstract

In vitro surface coatings are widely used to mimic the role of extracellular matrix in the *in vivo* environment. Different effects are reported for different surface coatings, however, some of these results are inconsistent across the literature. To explore the role of different surface coatings, we use a new modified stopper-based wound-healing assay, called a *stopper assay*, with two commonly used surface coatings: gelatin and poly-L-lysine (PLL). Our experimental data show the gap width decreases faster with the gelatin and PLL coatings. Similarly, the number of cells in certain subregions increases faster with these coatings. Unfortunately, neither of these observations provides definitive mechanistic insight into the role of the coatings. To provide such insight we calibrate the solution of the Fisher-Kolmogorov model to match the experimental data. Our parameter estimates indicate that both coatings significantly increase cell motility without affecting cell proliferation.

Key words: Wound healing assay; Stopper assay; Surface coating;
Fisher-Kolmogorov; Reaction-diffusion; Transport

* Corresponding author.

Email address: `w1.jin@qut.edu.au` (Wang Jin).

1 Introduction

In vitro surface coatings are used as a fundamental experimental approach to mimic and study the effect of the extracellular matrix (ECM) in the *in vivo* environment. It is important to include effects of the ECM in experimental studies because the ECM interacts with cells both physically and chemically, affects cell behaviour, and plays an important role in biological processes such as tissue development and cancer progression (Hay 2013; Horiguchi et al., 2012; Screen et al., 2015; Vedula et al., 2013). Popular choices of coating reagents include gelatin, poly-L-lysine (PLL), collagen, and fibronectin (Liberio et al., 2014; McCarthy et al., 1983; McIntosh et al., 1988). The precise role of surface coatings, however, remains unclear since experimental observations are inconsistent. For example, gelatin is thought to increase both cell motility and proliferation (McCarthy et al., 1983; McIntosh et al., 1988), while PLL can have the opposite effects (Liberio et al., 2014). In contrast, other studies suggest that PLL may have no impact on cell motility or proliferation (Fischer et al., 2007; Rangappa et al., 2000).

Among various types of *in vitro* experiments, wound-healing assays are widely used to study cell migration and cell proliferation under different conditions including the use of different surface coatings (Ascione et al., 2017; Liberio et al., 2014; Tremel et al., 2009). Wound-healing assays are initiated by creating a scratch in a monolayer of cells, followed by the observation of how the remaining cells migrate and proliferate to close the gap over time. This type of assay can be used to provide quantitative insight by measuring rates of the gap closure or measuring the increase in the numbers of cells in particular subregions of the experiment (Johnston et al., 2014; Liberio et al., 2014; McCarthy et al., 1983; Treloar and Simpson, 2013). However, these measurements alone cannot tease apart the intricate interplay between the effects of cell migration and cell proliferation that can sometimes lead to surprising results. For example, Barrandon and Green (1987) measure the temporal change in the numbers of cells in certain *in vitro* colonies and note a dramatic increase in cell numbers

31 when TGF- α is included. This increase in cell number is due to the interplay of
32 cell migration and cell proliferation, since TGF- α promotes migration, which
33 then in turn provides space for the cells to proliferate (Barrandon and Green,
34 1987).

35 Mathematical models have been applied to mimic both *in vitro* and *in vivo*
36 experiments to test biological hypotheses and to predict experimental out-
37 comes (Jin et al., 2018a; Jove et al., 2019; Nardini et al., 2016; Sheardown and
38 Cheng, 1996; Tam et al., 2019; Villella et al., 2019). One of the most com-
39 monly used models to study collective cell migration is the Fisher-Kolmogorov
40 model (Fisher, 1937; Maini et al., 2004; Sherratt and Murray, 1990; Simpson
41 et al., 2006). The Fisher-Kolmogorov model describes the interplay between
42 cell migration and cell proliferation by assuming (i) cells migrate according to
43 undirected linear diffusion, and (ii) cells proliferate logistically to a carrying
44 capacity density. In previous studies, the Fisher-Kolmogorov model has been
45 calibrated to match experimental data from *in vitro* wound-healing assays,
46 and has been used to provide mechanistic insight into the role of the initial
47 seeding density, the wound geometry, and the shape of the migrating front
48 (Jin et al., 2016; Jin et al., 2018b; Sengers et al., 2007).

49 In this work we apply a new modified stopper-based *in vitro* wound-healing
50 assay, called a *stopper assay*, to explore the role of two widely used surface
51 coatings: gelatin and PLL. Compared to other commercial experimental ap-
52 paratus (Liberio et al., 2014; Qi et al., 2019), one important feature of the
53 stopper assays is that we can study two different coating conditions simulta-
54 neously in one experimental well. This allows us to make direct comparisons
55 of how different coatings affect gap closure in the same field-of-view without
56 being concerned by potential differences caused by monitoring different exper-
57 imental wells. Our experimental data describes the gap width and the increase
58 in the numbers of cells in particular subregions in the experiment. This data
59 indicates that the gap closes faster, and the cell population increases faster in
60 the gelatin- and PLL-coated regions. By calibrating the Fisher-Kolmogorov
61 model to match the experimental data, we find that both gelatin and PLL

62 coatings significantly increase the cell diffusivity without affecting the rate of
63 cell proliferation.

64 2 Methods

65 2.1 *Experimental methods*

66 Stopper assays are performed in six-well experimental plates (Corning, USA),
67 in which each experimental well has a diameter of 35 mm. Schematics of the
68 stopper assays are illustrated in Figure 1. The lower semicircular surface of the
69 experimental well is covered with tape (8018, 3M) to form the uncoated control
70 area (Figure 1(a)). For the surface coating, sterile 0.1% (w/w) gelatin (Sigma,
71 USA) or 0.1 $\mu\text{g/mL}$ poly-L-lysine (Sigma, USA) prepared in 1X phosphate-
72 buffered saline (PBS) is added to the well and incubated at 37 °C for 30
73 min. After the excess liquid is aspirated completely, the tape is removed, with
74 only the upper semicircular surface of the well coated (Figure 1(a)). In the
75 remainder of this work, we refer to the upper and lower semicircular surfaces
76 of the experimental well as the *upper half* and the *lower half*, respectively.

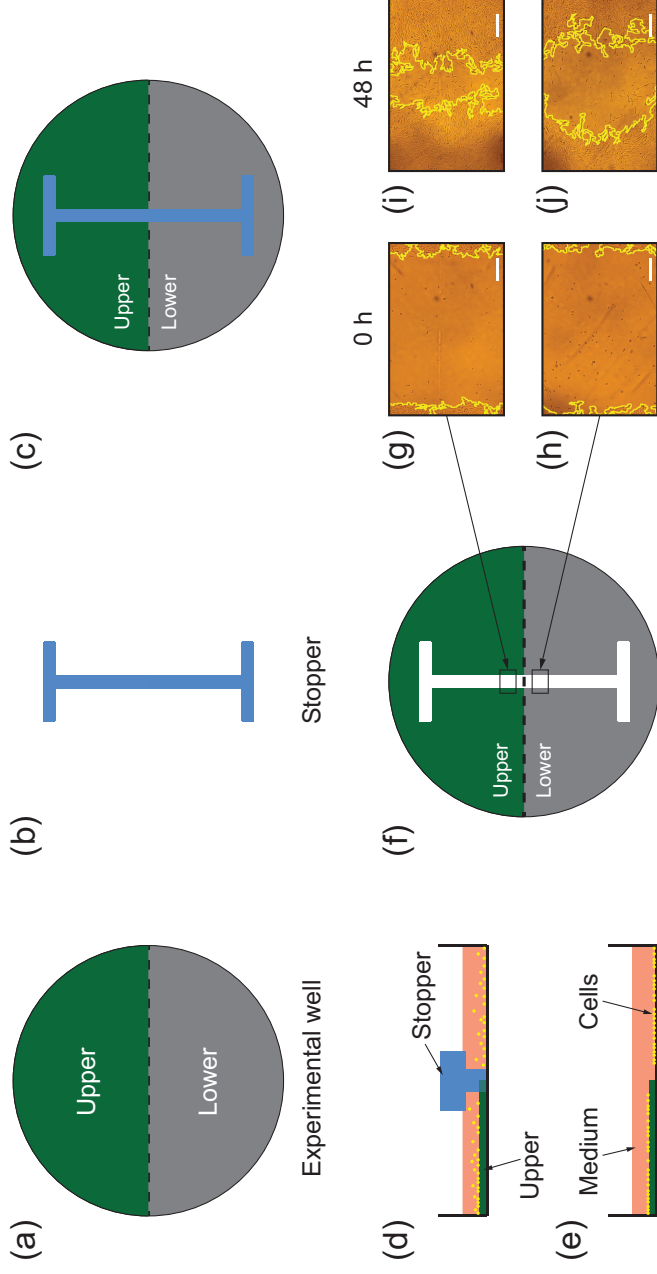


Fig. 1. Illustrations of *in vitro* stopper assays. (a) Experimental well in which the upper half is coated. (b) A stopper for creating the cell-free region. (c) Experimental well with a stopper placed in the middle. (d) Section of the stopper assay with a stopper in place. The thick green line indicates the upper half and the yellow dots indicate cells. (e) Section of the stopper assay after a cell monolayer is grown and the stopper is removed. (f) An illustration of how the data are retrieved from the stopper assay. The white space indicates the initially vacant area. The black rectangles correspond to regions where two experimental images are taken. (g)–(h) Experimental images taken at $t = 0$ h in the indicated upper and lower halves, shown in (f). (i)–(j) Experimental images taken at $t = 48$ h in the indicated upper and lower halves. The yellow line indicates edges of the gap. The scale bar corresponds to $500 \mu\text{m}$.

77 We perform the experiments with the mouse embryonic fibroblast cell line
78 NIH 3T3, purchased from the Bioresource Collection and Research Center
79 (BCRC), Taiwan. The cell culture medium consists of Dulbecco's Modified
80 Eagle's medium (DMEM, Gibco, USA) and 10% calf serum (CS, Invitrogen,
81 USA). Although the calf serum can adhere to the surface of the experimental
82 wells and potentially interact with surface coatings, many studies that use calf
83 serum do not consider this to be an explicit coating treatment (Gospodarowicz
84 et al., 1983; Liberio et al., 2014; Rangappa et al., 2000). Cells are incubated
85 in cell culture flasks (Corning, USA) under 5% CO₂ at 37 °C.

86 A customized I-shaped stopper (Figure 1(b)), made of polydimethylsiloxane
87 (PDMS, Dow Corning SylgardTM 184 Silicone Elastomer, USA), is placed
88 into the experimental well so that it is perpendicular to the boundary of
89 the upper and lower halves (Figure 1(c)). Approximately 2.5×10^5 cells are
90 seeded uniformly into the six-well experimental plates and incubated overnight
91 (Figure 1(d)). The stopper is then removed to create an initial gap (Figure
92 1(e)). After removing the stopper, cells are free to migrate and proliferate,
93 eventually leading to the closure of the initially vacant space in both the
94 upper and lower halves (Figure 1(g)-(i)). The gap width and the number of
95 cells in certain subregions are measured at five equally-spaced time points:
96 $t = 0, 12, 24, 36$, and 48 h. Each experiment is performed three times so that we
97 can extract data from each replicate and average the data across the replicates.
98 In this work we use data describing individual experimental replicates as well
99 as the averaged data. To distinguish these two types of the data, we use
100 superscripts on certain variables to indicate the individual replicate number,
101 and we use the variables with a tilde to indicate the averaged data.

102 Before presenting our experimental and modelling results, we now describe
103 some of the terminology we use to describe the experimental protocol and ex-
104 perimental data. Some experiments do not involve any coating at all, and we
105 refer to these experiments as *control* experiments. Other experiments involve
106 applying different coatings to the experimental well, of which the upper half is
107 coated with gelatin or PLL and the lower half is uncoated (Figure 1(f)). This

means that we have two different types of control assays: one type corresponds to the control experiments, and the other type corresponds to the uncoated regions in the coating experiments. In Section 3.1 we plot the average data for the control experiment as well as the average data in the upper and lower halves of the wells for the experiments with gelatin and PLL coatings. When we calibrate the solution of the Fisher-Kolmogorov model to match the experimental replicates in Section 3.3, we combine data from the two types of control assays which we refer to as the *regrouped control experiment*.

2.2 Edge detection and cell counting methods

We use ImageJ to detect edges of vacant areas and measure the gap areas from the experimental images at $t = 0, 12, 24, 36$, and 48 h (Schindelin et al., 2015; Simpson et al., 2013). Details of the methods are described in Jin et al. (2018b). Examples of experimental images, each of which has a length of $1960 \mu\text{m}$ and a width of $1288 \mu\text{m}$, with detected gap edges superimposed, are shown in Figure 2. In the remainder of this work we refer to the area contained in the experimental image as the *experimental field-of-view*, since these images show relatively small subregions within the entire experimental well (Simpson et al., 2018). Estimates of the gap width at each time point is calculated by taking the gap area divided by the width of the experimental field-of-view. This calculation is performed at each time point for each experimental replicate. Here we use $W^{(r)}(t)$ to denote the experimental measurement of the gap width for replicate r at time t . We then average the data to give $\widetilde{W}(t) = (1/R) \sum_{r=1}^R W^{(r)}(t)$, where R is the number of replicates. We report the sample mean as well as the variability across the replicates by calculating and reporting the sample standard deviation.

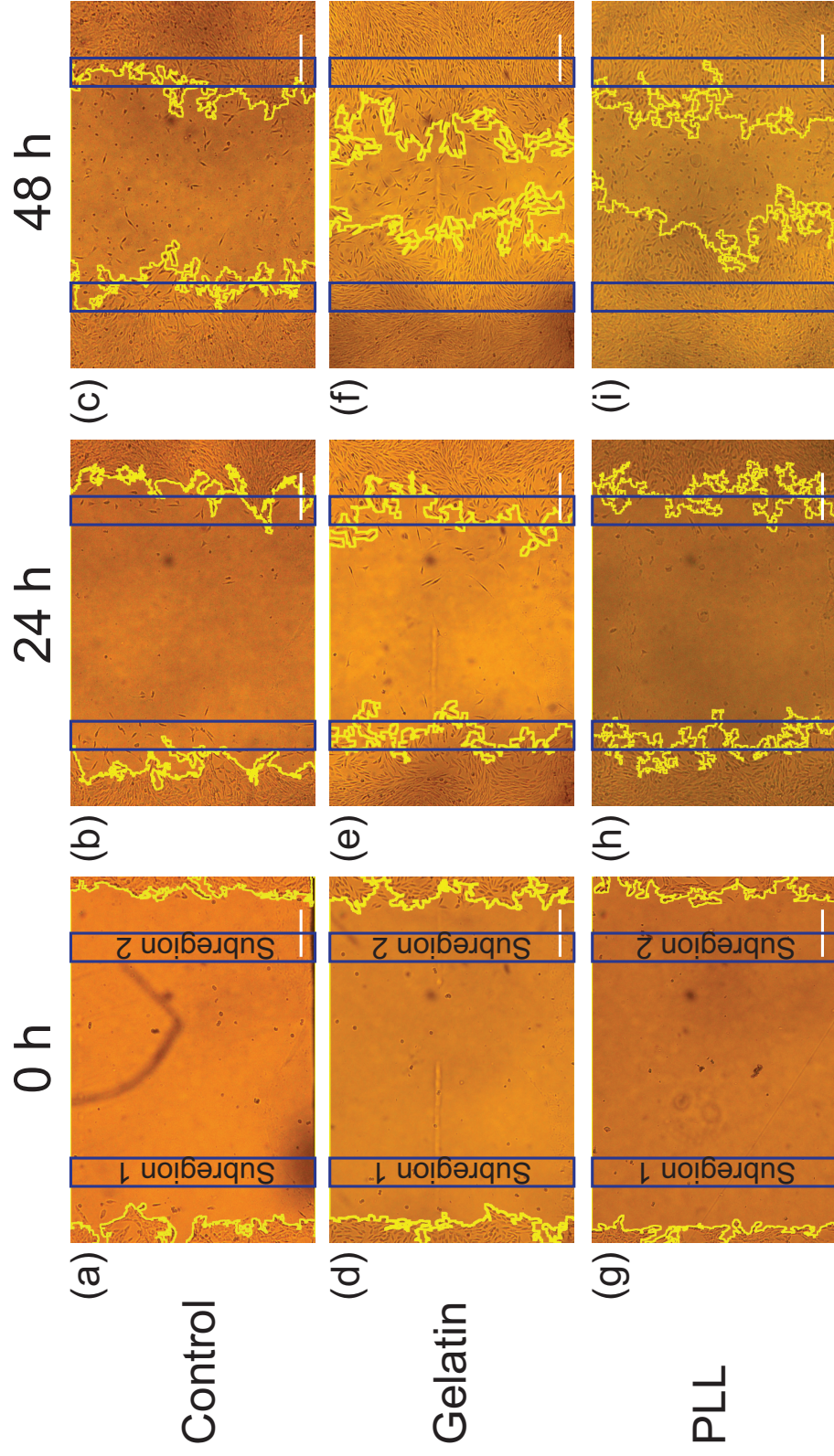


Fig. 2. **Experimental images at $t = 0$, 24, and 48 h from stopper assays.** (a)–(c) Experimental images of the control experiment. (d)–(f) Experimental images of the gelatin-coated experiments. (g)–(i) Experimental images of the PLL-coated experiments. All images show the experimental field-of-view in the upper half of the experimental well, indicated by the black arrow in Figure 1(f)–(g). The yellow line indicates the detected edge of the gap area produced by ImageJ. The rectangle highlighted in blue indicates the subregions in which cell numbers are counted over time. The scale bar corresponds to 500 μm .

133 We manually count the number of individual cells contained in two rectangular
 134 subregions at $t = 0, 12, 24, 36$, and 48 h. Each subregion, highlighted in blue
 135 in Figure 2, measures $1288 \mu\text{m} \times 150 \mu\text{m}$. The two subregions are located 300
 136 μm away from the left and right boundaries of the experimental field-of-view,
 137 respectively. For simplicity we refer to the left-most subregion as *Subregion*
 138 *1* and the right-most subregion as *Subregion 2*. These estimates are obtained
 139 at each time point for each experimental replicate. Here we use $N_1^{(r)}(t)$ and
 140 $N_2^{(r)}(t)$ to represent the experimental measurement of the number of cells
 141 within Subregion 1 and Subregion 2 for replicate r at time t , respectively.
 142 We then average the data to give $\widetilde{N}_1(t) = (1/R) \sum_{r=1}^R N_1^{(r)}(t)$, and $\widetilde{N}_2(t) =$
 143 $(1/R) \sum_{r=1}^R N_2^{(r)}(t)$.

144 Since the Subregion 1 and Subregion 2 are located symmetrically about the
 145 centre of the experimental field-of-view, we expect that the number of cells in
 146 each subregion will be approximately equal. Therefore, we average the num-
 147 ber of cells in the two subregions for each experimental replicate to give
 148 $N^{(r)}(t) = (N_1^{(r)}(t) + N_2^{(r)}(t)) / 2$. We also average this quantity across the
 149 experimental replicates to give $\widetilde{N}(t) = (\widetilde{N}_1(t) + \widetilde{N}_2(t)) / 2$. Again, we report
 150 these averaged quantities and we approximate the uncertainty in these quan-
 151 tities by calculating and reporting the sample standard deviation.

153 The Fisher–Kolmogorov model is a reaction–diffusion equation given by

$$\frac{\partial \bar{C}(x, y, t)}{\partial t} = \overbrace{D \nabla^2 \bar{C}(x, y, t)}^{\text{linear diffusion}} + \overbrace{\lambda \bar{C}(x, y, t) \left(1 - \frac{\bar{C}(x, y, t)}{K}\right)}^{\text{logistic growth}}, \quad (1)$$

154 on $0 \leq x \leq X$, $0 \leq y \leq Y$, where X and Y are the horizontal length and verti-
 155 cal height of the experimental field-of-view, respectively (see Figure 3(a)–(b)),
 156 and $t \geq 0$ is time. In this model $\bar{C}(x, y, t) \geq 0$ [cells/ μm^2] is the cell density,
 157 $D \geq 0$ [$\mu\text{m}^2/\text{h}$] is the cell diffusivity, $\lambda \geq 0$ [/h] is the cell proliferation rate,
 158 and $K > 0$ [cells/ μm^2] is the carrying capacity density. Since all cells, both
 159 inside and outside of the experimental field-of-view, are uniformly seeded we
 160 define our simulation domain to be a horizontal extension of the experimental
 161 field-of-view, by doubling its length to avoid boundary effects. Therefore, we
 162 solve Equation (1) on $-X/2 \leq x \leq 3X/2$, and $0 \leq y \leq Y$. Zero net flux
 163 boundary conditions are applied along the four boundaries (Jin et al. 2016).

164 Previously, Simpson (2009) showed that depth-averaging can be used to sim-
 165 plify two-dimensional reaction-diffusion models into one-dimensional reaction-
 166 diffusion models by averaging $\bar{C}(x, y, t)$ in the vertical direction,

$$C(x, t) = \frac{1}{Y} \int_0^Y \bar{C}(x, y, t) \, dy, \quad (2)$$

167 where $C(x, t)$ [cells/ μm^2] is the one-dimensional vertically averaged cell den-
 168 sity. To simplify Equation (1) we integrate both sides of the reaction–diffusion
 169 equation with respect to y , and then divide both sides by Y to obtain

$$\frac{\partial C}{\partial t} = D \frac{\partial^2 C}{\partial x^2} + \frac{D}{Y} \left(\frac{\partial C}{\partial y} \Big|_Y - \frac{\partial C}{\partial y} \Big|_0 \right) + \lambda C \left(1 - \frac{C}{K} \right). \quad (3)$$

170 We note that the second and third terms on the right side of Equation (3)
 171 vanish since $\partial C / \partial y = 0$ along the boundaries where $y = 0$ and $y = Y$.
 172 Therefore, Equation (3) reduces to

$$\frac{\partial C}{\partial t} = D \frac{\partial^2 C}{\partial x^2} + \lambda C \left(1 - \frac{C}{K} \right). \quad (4)$$

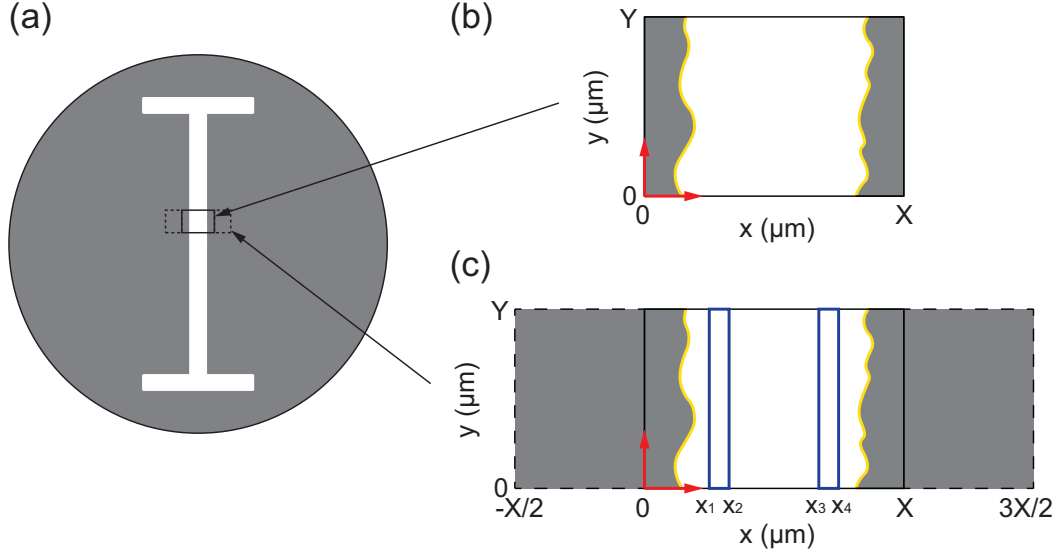


Fig. 3. **Schematics showing the entire experimental well, the experimental field-of-view, and the simulation domain.** (a) Entire experimental well. The white area shows the initial gap made by the stopper. The grey area shows the region where cells are uniformly seeded. (b) Experimental field-of-view, where $X = 1960 \mu\text{m}$, $Y = 1288 \mu\text{m}$ and the origin and coordinate system is shown in red. The yellow curve highlights the gap edges. (c) Simulation domain. The inner rectangular region (solid lines) shows the actual experimental field-of-view. The outer rectangular region (dashed lines) shows the extended simulation domain. The blue rectangular subregions indicate the areas where cell numbers are counted.

173 It is worth noting that simplifying a two-dimensional reaction-diffusion model
 174 into a vertically averaged one-dimensional model can introduce an error. How-
 175 ever, this error vanishes when the initial condition is uniform in the vertical
 176 direction (Simpson, 2009). Since the stopper assays do not involve any cell
 177 density gradients in the vertical direction, there is no error associated with
 178 averaging the two-dimensional reaction-diffusion equation into the simpler
 179 one-dimensional reaction-diffusion equation.

180 *2.3.1 Estimating gap width using the Fisher-Kolmogorov model*

181 One feature of the Fisher-Kolmogorov model is that its solutions do not have
 182 compact support (McCue et al., 2019). A level set $\epsilon \in [0, K]$, needs to be
 183 nominated to represent edges of the gap. The choice of ϵ also affects the com-
 184 putation of gap width, $\mathcal{W}(t)$. To estimate $\mathcal{W}(t)$ from the numerical solution
 185 of Equation (4), we calculate the x coordinates, x_l and x_r , at left and right
 186 side of the gap, respectively, which satisfies $C(x_l, t) = C(x_r, t) = \epsilon$. With this
 187 data the gap width is given by $\mathcal{W}(t) = x_r - x_l$, provided $x_r > x_l$. Otherwise
 188 $\mathcal{W}(t) = 0$. When we calibrate the mathematical model to a particular exper-
 189 imental replicate we use a superscript to denote the particular replicate. For
 190 example, $\mathcal{W}^{(r)}(t)$ denotes the gap width predicted by the model for experi-
 191 mental replicate r .

192 *2.3.2 Estimating the number of cells using the Fisher-Kolmogorov model*

193 The number of cells within Subregion 1 and Subregion 2 can be calculated by
 194 integrating the cell density, $C(x, t)$, over the two subregions, giving

$$\mathcal{N}_1(t) = Y \int_{x_1}^{x_2} C(x, t) dx, \quad \text{and} \quad \mathcal{N}_2(t) = Y \int_{x_3}^{x_4} C(x, t) dx, \quad (5)$$

195 where $C(x, t)$ is the cell density obtained by solving Equation (4) numerically.
 196 We further average $\mathcal{N}_1(t)$ and $\mathcal{N}_2(t)$ to give

$$\mathcal{N}(t) = \frac{\mathcal{N}_1(t) + \mathcal{N}_2(t)}{2}. \quad (6)$$

197 Again, when we calibrate the mathematical model to a particular experimental
 198 replicate we use a superscript to denote the particular replicate. For example,
 199 $\mathcal{N}^{(r)}(t)$ denotes the number of cells predicted by the model for experimental
 200 replicate r .

201 3 Results and discussion

202 3.1 Experimental estimates of $\widetilde{W}(t)$ and $\widetilde{N}(t)$

203 Using the methods described in Section 2.2, we obtain estimates of $\widetilde{W}(t)$
 204 and $\widetilde{N}(t)$ for the gelatin, PLL, and control experiments (Figure 4(a)–(b)).
 205 This average data indicates that $\widetilde{W}(t)$ decreases fastest for the gelatin-coated
 206 experiments and slowest for the control experiments. We also see similar trends
 207 in terms of $\widetilde{N}(t)$ data. Starting with $\widetilde{N}(0) = 0$ in all cases, the experiments
 208 with gelatin coating lead to the fastest increase in $\widetilde{N}(t)$ while the control
 209 experiments lead to the slowest increase in $\widetilde{N}(t)$.

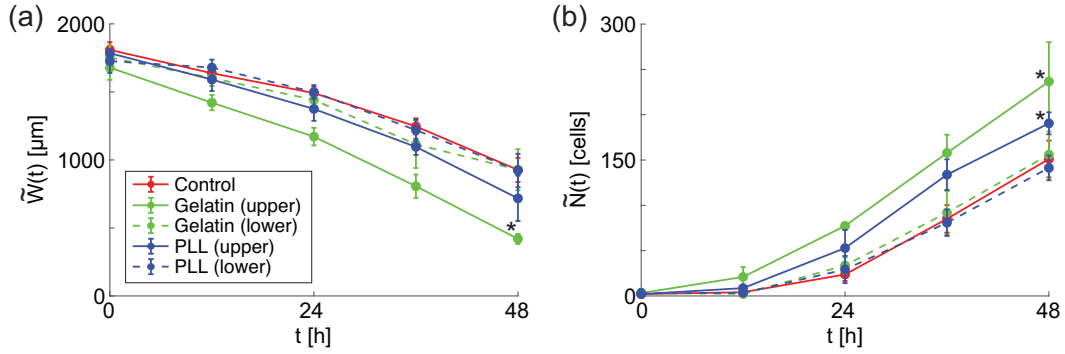


Fig. 4. **Time evolution of $\widetilde{W}(t)$ and $\widetilde{N}(t)$** (a) Time evolution of $\widetilde{W}(t)$ for the control, gelatin, and PLL experiments. (b) Time evolution of $\widetilde{N}(t)$ for the control, gelatin, and PLL experiments. Data points correspond to the sample mean and the error bars indicate the sample standard deviation. The asterisk indicates the data with which the null hypothesis is rejected at the 5% level.

210 To statistically identify the significance of difference in both the $\widetilde{W}(t)$ and $\widetilde{N}(t)$
 211 data between the control and coating experiments, we conduct a two-sample
 212 t-test for $\widetilde{W}(48)$ and $\widetilde{N}(48)$, respectively, with the null hypothesis that the
 213 data in the control and coating experiments comes from independent random
 214 samples from normal distributions with equal means and equal but unknown
 215 variances (De Winter, 2013). The null hypothesis is rejected at the 5 % level
 216 ($p < 0.05$) for the experiments with gelatin coating in the $\widetilde{W}(48)$ data, and for

the experiments with gelatin and PLL coatings in the $\widetilde{N}(48)$ data. We obtain much larger p values when considering results for the lower half of the wells in the gelatin- and PLL-coated experiments, where the surface is uncoated. This result confirms our assumption that the two different types of control experiments we consider lead to indistinguishable results.

In summary, our experimental data shows that different coatings lead to different estimates of $\widetilde{W}(t)$ and $\widetilde{N}(t)$. For example, both coatings lead to $\widetilde{N}(t)$ that increases faster than $\widetilde{N}(t)$ for the control experiments. One naive way to interpret this difference is that the coatings stimulate cell proliferation. However, as we will show in Section 3.3, when we carefully interpret the experimental data using the Fisher–Kolmogorov model it suggests that the coatings stimulate cell migration but not cell proliferation.

To match the number of cells data with the solution of the Fisher-Kolmogorov model, we integrate both sides of Equation (4) with respect to x across the two subregions to give

$$\frac{d\mathcal{N}_1}{dt} = \overbrace{-D \frac{\partial C}{\partial x} \Big|_{x_1}}^{\text{flux into the left boundary of Subregion 1}} + \overbrace{D \frac{\partial C}{\partial x} \Big|_{x_2}}^{\text{flux out of the right boundary of Subregion 1}} + \overbrace{\lambda \int_{x_1}^{x_2} C \left(1 - \frac{C}{K}\right) dx}_{\text{population change in Subregion 1 due to cell proliferation}}, \quad (7)$$

$$\frac{d\mathcal{N}_2}{dt} = \overbrace{-D \frac{\partial C}{\partial x} \Big|_{x_3}}^{\text{flux into the left boundary of Subregion 2}} + \overbrace{D \frac{\partial C}{\partial x} \Big|_{x_4}}^{\text{flux out of the right boundary of Subregion 2}} + \overbrace{\lambda \int_{x_3}^{x_4} C \left(1 - \frac{C}{K}\right) dx}_{\text{population change in Subregion 2 due to cell proliferation}}. \quad (8)$$

Equations (7)–(8) show that the rate of change of cell numbers in particular subregions is driven by a combination of the net flux of cells across the boundaries of the subregion and the effect of proliferation within the subregion. Therefore, the increase in $\mathcal{N}(t)$ is driven by both the migration term and the proliferation term in Equation (4). Similarly the decrease in the width of the gap, $\mathcal{W}(t)$, is also driven by the combined migration and proliferation terms in Equation (4). Without carefully interpreting the experimental data

239 using a mathematical model it could be very difficult to separate the effects
 240 of cell migration from cell proliferation in these kinds of experiments. We will
 241 now calibrate the solution of Equation (4) to match the data for individual
 242 replicates, but first we will estimate the carrying capacity density and the
 243 initial condition separately.

244 3.2 Specifying the carrying capacity density and the initial condition

245 We directly measure the carrying capacity density, K , from the experimental
 246 images (Supplementary Material). Direct counting of maximum cell densi-
 247 ties at the final time point of the experiments gives $K = 2.43 \pm 0.36 \times 10^{-3}$
 248 cells/ μm^2 . We find that our estimates of K are very similar for the control,
 249 PLL- and gelatin-coated experiments so we have pooled all these estimates
 250 together (Supplementary Material). Since we find that K does not vary sig-
 251 nificantly between different replicates or between different coating conditions,
 252 we treat K as a constant.

253 Unlike the carrying capacity density, we find that there are some differences
 254 in the details of the initial conditions in the various experimental replicates.
 255 Therefore we specify a different initial condition for each replicate by counting
 256 cells away from the initial gap. The initial condition for each replicate is given
 257 by

$$C^{(r)}(x, 0) = \begin{cases} \mathcal{C}_0^{(r)}, & x \leq (X - W^{(r)}(0)) / 2, \\ 0 & (X - W^{(r)}(0)) / 2 < x < (X + W^{(r)}(0)) / 2, \\ \mathcal{C}_0^{(r)}, & x \geq (X + W^{(r)}(0)) / 2, \end{cases} \quad (9)$$

258 where $W^{(r)}(0)$ is the initial gap width in experimental replicate r , and $\mathcal{C}_0^{(r)}$
 259 is the cell density away from the initial gap in experimental replicate r . We
 260 extract these quantities from each experimental replicate and report them in
 261 the Supplementary Material document.

262 3.3 Calibrating the cell diffusivity and the cell proliferation rate

263 In this section we calibrate the solution of Equation (4) to match both the
 264 $W^{(r)}(t)$ and $N^{(r)}(t)$ data from each individual experimental replicate. We
 265 solve Equation (4) using a finite difference method, with our measurements
 266 of $C^{(r)}(x, 0)$ and K (Supplementary Material). In Figure 5(a)–(c) we plot
 267 the solution of Equation (4), $C(x, t)$ at $t = 0, 12, 24, 36$, and 48 h, for repli-
 268 cate 2 of the regrouped control, and experiments with gelatin and PLL coat-
 269 ings, respectively. Using these solutions we compute $\mathcal{W}(t)$ and $\mathcal{N}(t)$, and with
 270 these estimates we calibrate D , λ and ϵ using MATLAB’s *lsqcurvefit* algo-
 271 rithm (MathWorks, 2020) to provide the best match to the experimental data
 272 (Supplementary Material). We use a least-squares measure of the discrepancy
 273 between the data and the model solution, given by

$$E^{(r)}(D, \lambda, \epsilon) = \sum_{j=1}^5 \left[\frac{\mathcal{W}(t_j) - W^{(r)}(t_j)}{W_{\max}^{(r)}} \right]^2 + \left[\frac{\mathcal{N}(t_j) - N^{(r)}(t_j)}{N_{\max}^{(r)}} \right]^2, \quad (10)$$

274 where j is an index indicating the time points, and $W_{\max}^{(r)}$ and $N_{\max}^{(r)}$ are the
 275 largest gap width and number of cells in experimental replicate r , respectively.
 276 For the experiments with gelatin and PLL coatings, we have $r = 1, 2$, and
 277 3 , while for the regrouped control experiment, $r = 1, 2, \dots, 9$. Equation (10)
 278 measures the difference between the model predictions and experimental data,
 279 both scaled by the maximum value in the experimental observations. This
 280 approach of scaling normalises the two different types of the data so that both
 281 of them are in the same order of magnitude. Calibrating the solution of the
 282 Fisher-Kolmogorov model to match the data allows us to estimate values of D ,
 283 λ and ϵ that minimise $E^{(r)}$, and we denote these estimates using an overbar,
 284 $\bar{D}^{(r)}$, $\bar{\lambda}^{(r)}$ and $\bar{\epsilon}^{(r)}$ (Supplementary Material). Since these estimates do not vary
 285 too much across the different replicates, we average them across the replicates
 286 to give \bar{D} , $\bar{\lambda}$, $\bar{\epsilon}$, together with estimates of variability across the replicates in
 287 Table 1.

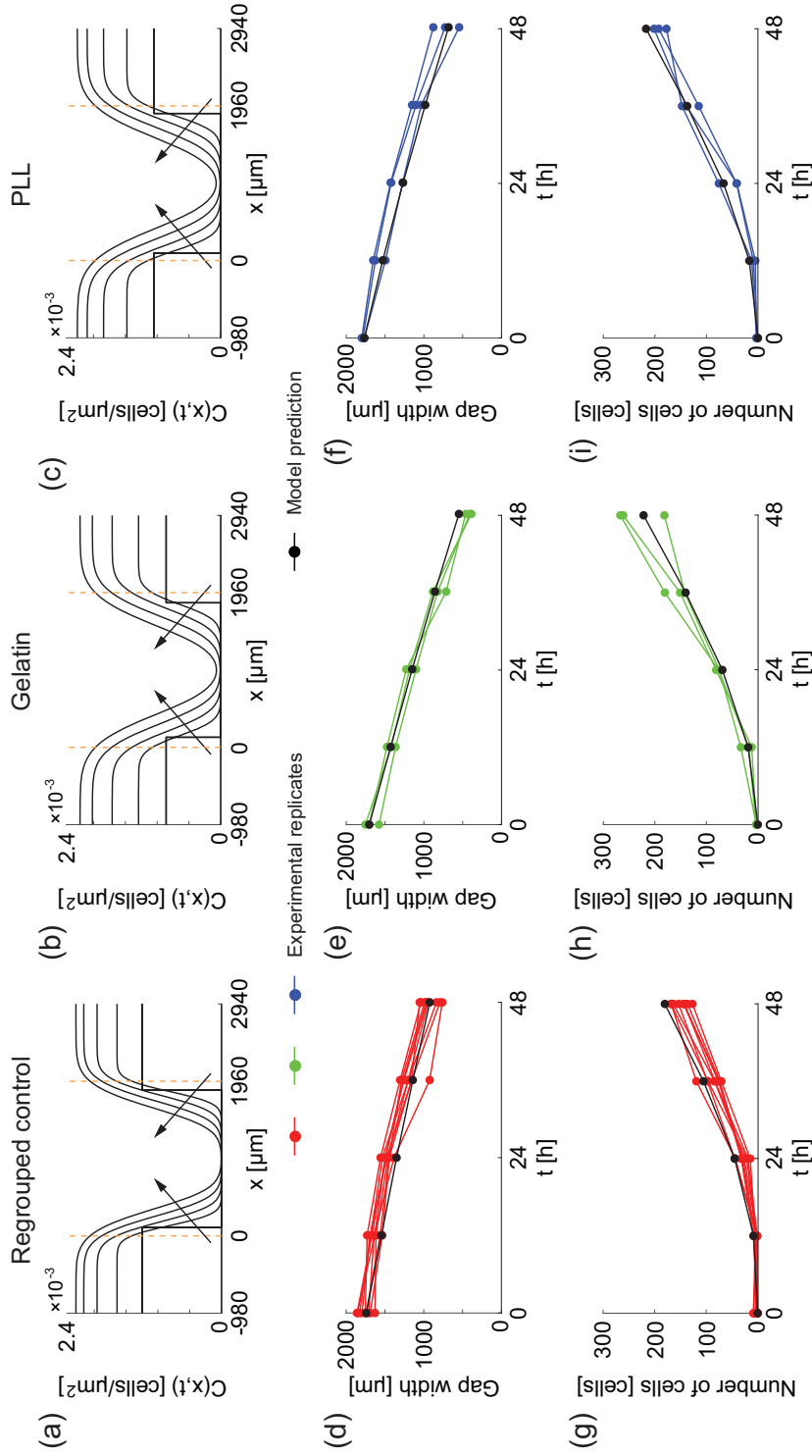


Fig. 5. Comparing calibrated solutions of the Fisher-Kolmogorov model and the experimental data. (a)–(c) Numerical solutions of Equation (4) at $t = 0, 12, 24, 36$, and 48 h, using \bar{D} and $\bar{\lambda}$, with $C^{(2)}(x, 0)$ and $W^{(2)}(0)$ for experimental replicate 2. The arrow indicates the direction of increasing t . The orange dashed vertical lines indicate the experimental field-of-view. (d)–(f) Time evolution of $\mathcal{W}^{(2)}(t)$ from the calibrated solution of Equation (4) superimposed on the data, $W^{(r)}(t)$, $r = 1, \dots, R$. (g)–(i) Time evolution of $\mathcal{N}(t)$ from the calibrated solution of Equation (4) superimposed on the data, $N^{(r)}(t)$, $r = 1, \dots, R$. In (d), (g), $R = 9$. In (e), (f), (h), (i), $R = 3$.

Table 1

Estimates of \bar{D} , $\bar{\lambda}$, and $\bar{\epsilon}$ from individual experimental data. All parameter estimates are given to two significant figures.

	\bar{D} ($\mu\text{m}^2/\text{h}$)	$\bar{\lambda}$ (/h)	$\bar{\epsilon}$ (% of K)
Control	600 ± 240	0.057 ± 0.0061	17 ± 2.7
Gelatin	1000 ± 140	0.061 ± 0.019	12 ± 2.9
PLL	1000 ± 390	0.059 ± 0.012	17 ± 2.9

Our estimates of \bar{D} , $\bar{\lambda}$ and $\bar{\epsilon}$ are within previously reported ranges for fibroblast cells (Jin et al., 2018b; Simpson et al., 2013; Tremel et al., 2009). Comparing estimates of \bar{D} and $\bar{\lambda}$ indicates that both the gelatin and PLL coatings stimulate cell migration by about 70% compared to the regrouped control experiment. However, the proliferation rate $\bar{\lambda}$ does not vary over the three groups. Therefore, we find that gelatin and PLL coatings lead to increased cell motility, whereas neither coatings have any significant impact on cell proliferation.

Furthermore, our estimates of \bar{D} for the gelatin and PLL coatings are very similar, suggesting that the impact of gelatin and PLL coatings on cell motility is similar. Results in Figure 5(d)–(i) show $\mathcal{W}^{(2)}(t)$ and $\mathcal{N}^{(2)}(t)$ obtained using the calibrated parameter values, superimposed with the $W^{(r)}(t)$ and $N^{(r)}(t)$ data for the individual experimental replicates. These results confirm that the calibrated solution of the Fisher–Kolmogorov model is consistent with the experimental data.

4 Conclusions

In vitro experimental approaches often study the effect of surface coatings simply by comparing images of experiments with coatings to control experiments without coatings. While such comparisons provide information about the net effect of the coating, the simple observations do not provide any insight into

308 how the coating affects the cell-level mechanisms. For example, observing that
309 a particular coating increases the rate of gap closure provides no insight into
310 whether the increase in the closure rate is driven by an increase in cell motility,
311 an increase in cell proliferation, or a combined increase in cell motility and
312 cell proliferation.

313 In this work we take a different, more quantitative approach to assess the
314 impact of different coatings on *in vitro* wound-healing experiments. We are
315 motivated to take this approach because we aim to understand how different
316 coatings affect different mechanisms. We consider three types of experiments
317 including control experiments without any coating as well as experiments with
318 gelatin and PLL coatings. In each experiment we extract two types of data:
319 (i) the gap width as a function of time; and (ii) the number of cells contained
320 within particular subregions as a function of time. By carefully calibrating
321 the solution of the Fisher–Kolmogorov model to match both types of data we
322 obtain estimates of the cell diffusivity, D , and the cell proliferation rate, λ .
323 Comparing estimates of D and λ between the control experiments and the
324 experiments with gelatin and PLL coatings indicates that these two coatings
325 increase cell migration by approximately 70% whereas the coatings have neg-
326 ligible impact on cell proliferation.

327 Overall, our results suggest that care ought to be taken when interpreting the
328 experimental data. For example, simply counting the number of cells within
329 particular subregions of the experiment shows that the number of cells in-
330 creases more dramatically in the experiments with PLL and gelatin coatings.
331 Our modelling suggests that this increase in cell number is driven by the coat-
332 ings stimulating cell migration without influencing the rate of cell proliferation.
333 This conclusion might not be obvious without interpreting our experimental
334 data with a mechanistic mathematical model.

335 *Acknowledgments.* We are supported by the Australian Research Council (DP170100474)
336 and the Taiwan Ministry of Science and Technology (MOST 106-2313-B-002-
337 031-MY3, MOST 107-2221-E-030-001-MY2). Wang Jin is supported by a QUT

338 Vice Chancellor’s Research Fellowship. We thank two reviewers for their help-
339 ful comments.

340 References

- 341 [1] Ascione F, Caserta S, Guido S, 2017. The wound healing assay revisited: A
342 transport phenomena approach. *Chem Eng Sci.* 160, 200–209.
- 343 [2] Barrandon Y, Green H, 1987. Cell migration is essential for sustained growth
344 of keratinocyte colonies: the roles of transforming growth factor- α and epidermal
345 growth factor. *Cell.* 50, 1131-1137.
- 346 [3] De Winter JC, 2013. Using the Student’s t-test with extremely small sample
347 sizes. *Pract Assess, Res Eval.* 18, 10.
- 348 [4] Fischer S, Uetz-von Allmen E, Waeckerle-Men Y, Groettrup M, Merkle HP,
349 Gander B, 2007. The preservation of phenotype and functionality of dendritic cells
350 upon phagocytosis of polyelectrolyte-coated PLGA microparticles. *Biomaterials.*
351 28, 994-1004.
- 352 [5] Fisher RA, 1937. The wave of advance of advantageous genes. *Ann Eugen.* 7,
353 353–369.
- 354 [6] Gospodarowicz D, Gonzalez R, Fujii DK, 1983. Are factors originating from
355 serum, plasma, or cultured cells involved in the growth-promoting effect of the
356 extracellular matrix produced by cultured bovine corneal endothelial cells? *J Cell*
357 *Physiol.* 114, 191-202.
- 358 [7] Hay ED (Ed.), 1991. *Cell Biology of Extracellular Matrix.* Springer Science &
359 Business Media, New York.
- 360 [8] Horiguchi M, Ota M, Rifkin DB, 2012. Matrix control of transforming growth
361 factor- β function. *J Biochem.* 152, 321-329.
- 362 [9] Jin W, Shah ET, Penington CJ, McCue SW, Chopin LK, Simpson MJ, 2016.
363 Reproducibility of scratch assays is affected by the initial degree of confluence:
364 Experiments, modelling and model selection. *J Theor Biol.* 390, 136–145.

- [10] Jin W, Liang X, Brooks A, Futrega K, Liu X, Doran MR, Simpson MJ, Roberts MS, Wang H, 2018a. Modelling of the SDF-1/CXCR4 regulated *in vivo* homing of therapeutic mesenchymal stem/stromal cells in mice. PeerJ. 6, e6072.
- [11] Jin W, Lo KY, Chou SE, McCue SW, Simpson MJ, 2018b. The role of initial geometry in experimental models of wound closing. Chem Eng Sci. 179, 221-226.
- [12] Johnston ST, Simpson MJ, McElwain DLS, 2014. How much information can be obtained from tracking the position of the leading edge in a scratch assay? J R Soc Interface. 11, 20140325.
- [13] Jones LJ, Gray M, Yue ST, Haugland RP, Singer VL, 2001. Sensitive determination of cell number using the CyQUANT[®] cell proliferation assay. J Immunol Methods. 254, 85-98.
- [14] Jove M, Spencer JA, Hubbard ME, Holden EC, O'Dea RD, Brook BS, Phillips RM, Smye SW, Loadman PM, Twelves CJ, 2019. Cellular uptake and efflux of palbociclib *in vitro* in single cell and spheroid models. J Pharmacol Exp Ther. 370, 242-251.
- [15] Liang CC, Park AY, Guan JL, 2007. *In vitro* scratch assay: a convenient and inexpensive method for analysis of cell migration *in vitro*. Nat Protoc. 2, 329-333.
- [16] Liberio MS, Sadowski MC, Soekmadji C, Davis RA, Nelson CC, 2014. Differential effects of tissue culture coating substrates on prostate cancer cell adherence, morphology and behavior. PLOS ONE. 9, e112122.
- [17] Maini PK, McElwain DLS, Leavesley DI, 2004. Travelling waves in a wound healing assay. Appl Math Lett. 17, 575-580.
- [18] MathWorks. Lsqcurvefit.
<https://au.mathworks.com/help/optim/ug/lsqcurvefit.html> (Accessed: Feb 2020).
- [19] McCarthy JB, Palm SL, Furcht LT, 1983. Migration by haptotaxis of a Schwann cell tumor line to the basement membrane glycoprotein laminin. J Cell Biol. 97, 772-777.
- [20] McCue SW, Jin W, Moroney TJ, Lo KY, Chou SE, Simpson MJ, 2019. Hole-closing model reveals exponents for nonlinear degenerate diffusivity functions in cell biology. Physica D. 398, 130-140.

- 396 [21] McIntosh LC, Muckersie L, Forrester JV, 1988. Retinal capillary endothelial
397 cells prefer different substrates for growth and migration. *Tissue Cell.* 20, 193-
398 209.
- 399 [22] Nardini JT, Chapnick DA, Liu X, Bortz DM, 2016. Modeling keratinocyte
400 wound healing dynamics: Cell-cell adhesion promotes sustained collective
401 migration. *J Theor Biol.* 400, 103-117.
- 402 [23] Qi M, Darviot C, Patskovsky S, Meunier M, 2019. Cost-effective side-
403 illumination darkfield nanoplasmonic marker microscopy. *Analyst.* 144, 1303-1308.
404
- 405 [24] Rangappa N, Romero A, Nelson KD, Eberhart RC, Smith GM, 2000. Laminin-
406 coated poly (L-lactide) filaments induce robust neurite growth while providing
407 directional orientation. *J Biomed Mater Res.* 51, 625-634.
- 408 [25] Schindelin J, Rueden CT, Hiner MC, Eliceiri KW, 2015. The ImageJ ecosystem:
409 An open platform for biomedical image analysis. *Mol Reprod Dev.* 82, 518-529.
- 410 [26] Screen HR, Berk DE, Kadler KE, Ramirez F, Young MF, 2015. Tendon
411 functional extracellular matrix. *J Orthop Res.* 33, 793-799.
- 412 [27] Sengers BG, Please CP, Oreffo RO, 2007. Experimental characterization
413 and computational modelling of two-dimensional cell spreading for skeletal
414 regeneration. *J R Soc Interface.* 4, 1107-1117.
- 415 [28] Sheardown H, Cheng YL, 1996. Mechanisms of corneal epithelial wound healing.
416 *Chem Eng Sci.* 51, 4517-4529.
- 417 [29] Sherratt JA, Murray JD, 1990. Models of epidermal wound healing. *P Roy Soc*
418 *Lond B Bio.* 241, 29-36.
- 419 [30] Simpson MJ, Landman KA, Hughes BD, Newgreen DF, 2006. Looking inside
420 an invasion wave of cells using continuum models: proliferation is the key. *J Theor*
421 *Biol.* 243, 343-360.
- 422 [31] Simpson MJ, 2009. Depth-averaging errors in reactive transport modeling.
423 *Water Resour Res.* 45, W02505.

- 424 [32] Simpson MJ, Treloar KK, Binder BJ, Haridas P, Manton KJ, Leavesley DI,
425 McElwain DLS, Baker RE, 2013. Quantifying the roles of cell motility and cell
426 proliferation in a circular barrier assay. *J R Soc Interface*. 10, 20130007.
- 427 [33] Simpson MJ, Jin W, Vittadello ST, Tambyah TA, Ryan JM, Gunasingh G,
428 Haass NK, McCue SW, 2018. Stochastic models of cell invasion with fluorescent
429 cell cycle indicators. *Physica A*. 510, 375-386.
- 430 [34] Tam A, Green JE, Balasuriya S, Tek EL, Gardner JM, Sundstrom JF, Jiranek
431 V, Binder BJ, 2019. A thin-film extensional flow model for biofilm expansion by
432 sliding motility. *P R Soc A*. 475, 20190175.
- 433 [35] Treloar KK, Simpson MJ, 2013. Sensitivity of edge detection methods for
434 quantifying cell migration assays. *PLOS ONE*. 8, e67389.
- 435 [36] Tremel A, Cai A, Tirtaatmadja N, Hughes BD, Stevens GW, Landman KA,
436 O'Connor AJ, 2009. Cell migration and proliferation during monolayer formation
437 and wound healing. *Chem Eng Sci*. 64, 247–253.
- 438 [37] Vedula SR, Ravasio A, Lim CT, Ladoux B, 2013. Collective cell migration: a
439 mechanistic perspective. *Physiology*. 28, 370-379.
- 440 [38] Villella VR, Venerando A, Cozza G, Esposito S, Ferrari E, Monzani R, Spinella
441 MC, Oikonomou V, Renga G, Tosco A, Rossin F, Guido S, Silano M, Garaci E,
442 Chao Y, Grimm C, Luciani A, Romani L, Piacentini M, Raia V, Kroemer G,
443 Maiuri L, 2019. A pathogenic role for cystic fibrosis transmembrane conductance
444 regulator in celiac disease. *EMBO J*. 38, e100101.

Supplementary Material: Quantifying the role of different surface coatings in experimental models of wound healing

Wang Jin ^{a,b,*}, Kai-Yin Lo ^c, Yung-Shin Sun ^d, Ya-Han Ting ^c,
Matthew J Simpson ^a,

^a*School of Mathematical Sciences, Queensland University of Technology (QUT),
Brisbane, Queensland 4000, Australia.*

^b*ARC Centre of Excellence for Mathematical and Statistical Frontiers, QUT,
Brisbane, Queensland 4000, Australia.*

^c*Department of Agricultural Chemistry, National Taiwan University,
Taipei 10617, Taiwan.*

^d*Department of Physics, Fu-Jen Catholic University, Taipei 242, Taiwan.*

* Corresponding author.

Email address: w1.jin@qut.edu.au (Wang Jin).

Contents

1	Numerical methods for solving the Fisher-Kolmogorov model	3
2	Model calibration and additional parameter estimates data	4
3	Experimental data describing the carrying capacity density, the initial cell density, and the initial gap width	9
4	Experimental data for individual replicates	13
	References	24

1 Numerical methods for solving the Fisher-Kolmogorov model

The one-dimensional Fisher-Kolmogorov equation is of the form

$$\frac{\partial C}{\partial t} = D \frac{\partial^2 C}{\partial x^2} + \lambda C \left(1 - \frac{C}{K}\right), \quad (\text{S1})$$

on $-980 \leq x \leq 2940 \mu\text{m}$, where D [$\mu\text{m}^2/\text{h}$] is the cell diffusivity, λ [$1/\text{h}$] is the cell proliferation rate, and K [$\text{cells}/\mu\text{m}^2$] is the carrying capacity density. To numerically solve Equation (S1), the spatial domain is discretised into M nodes using a central difference approximation with uniform spacing δx . Here we denote C_i as the cell density at a discretised node i , where $i = 1, 2, 3, \dots, M$. The discretisation for the internal nodes at time t is as follows

$$\frac{dC_i(t)}{dt} = \frac{D}{\delta x^2} \left(C_{i+1}(t) - 2C_i(t) + C_{i-1}(t) \right) + \lambda C_i(t) \left(1 - \frac{C_i(t)}{K} \right), \quad (\text{S2})$$

for $i = 2, \dots, M - 1$. We apply zero net flux boundary condition at both boundaries, i.e., $C_2 = C_1$ and $C_M = C_{M-1}$. The initial condition is obtained by measuring cell densities from the experimental images at $t = 0$ h, with the average data and data for individual replicates given in Table S5 and Table S16, respectively. The resulting system of nonlinear ordinary differential equations is integrated using a backward Euler method with constant time step δt , which leads to a system of coupled nonlinear algebraic equations linearised and solved using the Thomas algorithm, with absolute tolerance η (Morton and Mayers, 2005). For all results presented in the main manuscript as well as the supplementary material, we choose $\delta x = 0.5 \mu\text{m}$, $\delta t = 0.1$ h, and $\eta = 1 \times 10^{-5}$ so that our results are grid-independent.

2 Model calibration and additional parameter estimates data

We numerically solve the one-dimensional Fisher-Kolmogorov model (Equation (S1)) using a finite difference method, with $C^{(r)}(x, 0)$ and K measured from the experimental images. Using the numerical methods introduced in Section 1, we obtain the density profiles at $t = 0, 12, 24, 36$, and 48 h. We then compute $\mathcal{W}(t)$ and $\mathcal{N}(t)$, and with these estimates we calibrate D and λ for the regrouped control, gelatin, and PLL experiments. We systematically vary ϵ , from $0.01K - 0.25K$, to identify the level set that minimises the least-squares measure of the discrepancy between the data and the model solution, given in Equation (10) in the main manuscript.

To consider the variation in the parameter estimates, we calibrate the solution of Equation (S1) to match the $W^{(r)}(t)$ and $N^{(r)}(t)$ data from each individual replicate. We find that each case appears to have a well-defined minimum, from which we estimate $\bar{D}^{(r)}$, $\bar{\lambda}^{(r)}$, and $\bar{\epsilon}^{(r)}$. We then average them across the replicates to give \bar{D} , $\bar{\lambda}$, and $\bar{\epsilon}$, which are listed in Table 1 in the main manuscript. In this supplementary material, we show histograms of the parameter estimates of the cell diffusivity $\bar{D}^{(r)}$ and proliferation rate $\bar{\lambda}^{(r)}$ for individual replicates in Figure S1. The estimated parameter values for individual replicates are listed in Table S1 - Table S3.

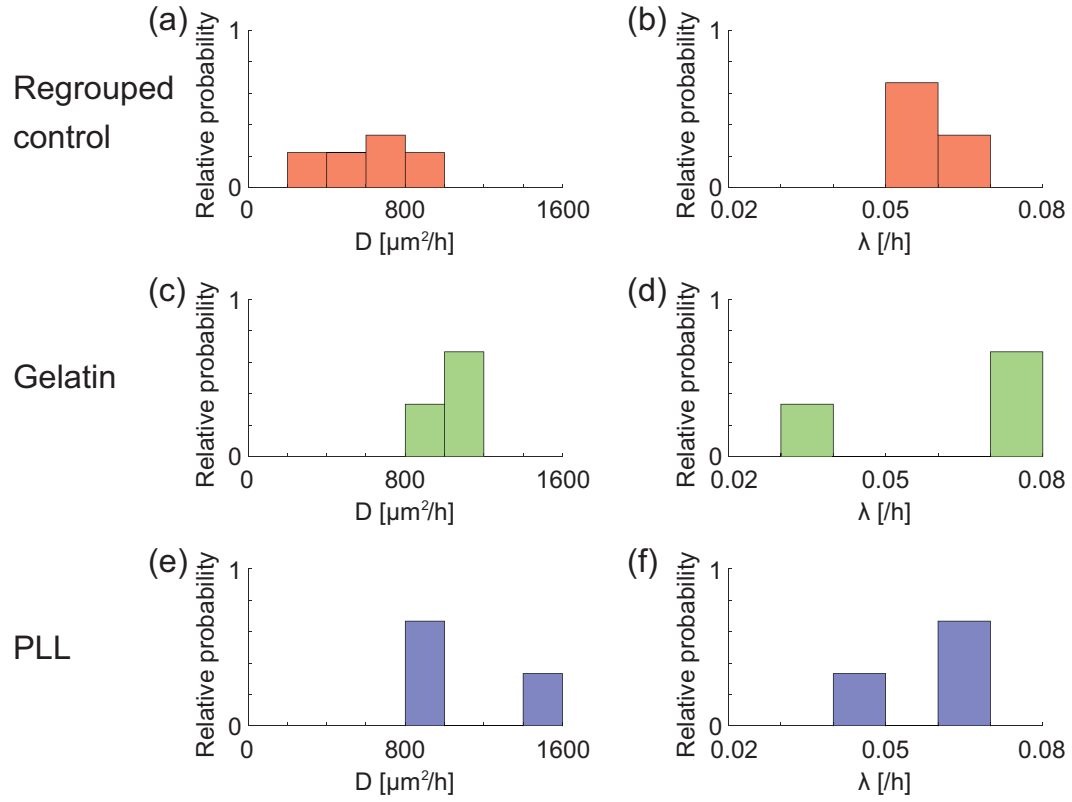


Fig. S1. **Histograms of parameter estimates of the cell diffusivity $\bar{D}^{(r)}$ and proliferation rate $\bar{\lambda}^{(r)}$.** The three rows correspond to the parameter estimates for the regrouped control, gelatin, and PLL experiments, respectively.

Table S1

Estimates of \bar{D} and $\bar{\lambda}$ for individual replicates in the regrouped control experiment. All parameter estimates are given to two significant figures. The red column in each replicate indicates the level set which gives the minimum least-squares measure.

Regrouped control		Level set ϵ (% of K)					
		1	5	10	15	20	25
Replicate 1	$\bar{D}^{(1)}$ [$\mu\text{m}^2/\text{h}$]	220	370	500	610	660	660
	$\bar{\lambda}^{(1)}$ [/h]	0.12	0.088	0.075	0.068	0.066	0.066
	$E^{(1)}$ ($\times 10^{-2}$)	13	5.8	2.7	1.4	1.4	2.5
Replicate 2	$\bar{D}^{(2)}$ [$\mu\text{m}^2/\text{h}$]	180	290	380	460	490	500
	$\bar{\lambda}^{(2)}$ [/h]	0.099	0.072	0.060	0.054	0.051	0.051
	$E^{(2)}$ ($\times 10^{-2}$)	12	4.9	1.8	0.53	0.43	1.2
Replicate 3	$\bar{D}^{(3)}$ [$\mu\text{m}^2/\text{h}$]	260	440	590	720	760	710
	$\bar{\lambda}^{(3)}$ [/h]	0.11	0.080	0.068	0.061	0.060	0.063
	$E^{(3)}$ ($\times 10^{-2}$)	14	6.0	2.3	0.85	1.1	2.7
Replicate 4	$\bar{D}^{(4)}$ [$\mu\text{m}^2/\text{h}$]	210	350	490	620	680	660
	$\bar{\lambda}^{(4)}$ [/h]	0.13	0.094	0.079	0.070	0.067	0.069
	$E^{(4)}$ ($\times 10^{-2}$)	12	5.4	2.1	0.71	0.56	1.5
Replicate 5	$\bar{D}^{(5)}$ [$\mu\text{m}^2/\text{h}$]	160	250	320	370	390	380
	$\bar{\lambda}^{(5)}$ [/h]	0.087	0.066	0.056	0.051	0.049	0.051
	$E^{(5)}$ ($\times 10^{-2}$)	9.6	3.6	1.1	0.36	0.63	1.6
Replicate 6	$\bar{D}^{(6)}$ [$\mu\text{m}^2/\text{h}$]	280	470	660	800	910	890
	$\bar{\lambda}^{(6)}$ [/h]	0.086	0.066	0.057	0.053	0.051	0.053
	$E^{(6)}$ ($\times 10^{-2}$)	14	6.5	3.5	2.9	4.1	7.1
Replicate 7	$\bar{D}^{(7)}$ [$\mu\text{m}^2/\text{h}$]	160	280	360	430	450	460
	$\bar{\lambda}^{(7)}$ [/h]	0.11	0.077	0.066	0.060	0.058	0.058
	$E^{(7)}$ ($\times 10^{-2}$)	16	7.9	4.0	2.2	1.6	1.9
Replicate 8	$\bar{D}^{(8)}$ [$\mu\text{m}^2/\text{h}$]	110	160	190	210	200	210
	$\bar{\lambda}^{(8)}$ [/h]	0.092	0.070	0.061	0.057	0.059	0.059
	$E^{(8)}$ ($\times 10^{-2}$)	8.2	4.1	2.6	2.2	2.3	2.8
Replicate 9	$\bar{D}^{(9)}$ [$\mu\text{m}^2/\text{h}$]	300	500	770	1000	1200	1100
	$\bar{\lambda}^{(9)}$ [/h]	0.093	0.072	0.059	0.052	0.050	0.052
	$E^{(9)}$ ($\times 10^{-2}$)	18	8.4	3.4	1.1	1.2	3.7

Table S2

Estimates of \bar{D} and $\bar{\lambda}$ for individual replicates in the gelatin experiment. All parameter estimates are given to two significant figures. The red column in each replicate indicates the level set which gives the minimum least-squares measure.

Gelatin		Level set ϵ (% of K)				
		1	5	10	15	20
Replicate 1	$\bar{D}^{(1)}$ [$\mu\text{m}^2/\text{h}$]	360	590	830	1100	1400
	$\bar{\lambda}^{(1)}$ [/h]	0.11	0.088	0.078	0.071	0.066
	$E^{(1)}$ ($\times 10^{-2}$)	6.8	2.4	0.89	0.62	1.3
Replicate 2	$\bar{D}^{(2)}$ [$\mu\text{m}^2/\text{h}$]	340	560	830	1100	1500
	$\bar{\lambda}^{(2)}$ [/h]	0.10	0.083	0.073	0.067	0.061
	$E^{(2)}$ ($\times 10^{-2}$)	6.0	2.4	1.3	1.3	2.4
Replicate 3	$\bar{D}^{(3)}$ [$\mu\text{m}^2/\text{h}$]	360	650	1000	1500	2400
	$\bar{\lambda}^{(3)}$ [/h]	0.059	0.046	0.039	0.034	0.031
	$E^{(3)}$ ($\times 10^{-2}$)	8.3	3.2	2.1	3.1	5.8

Table S3

Estimates of \bar{D} and $\bar{\lambda}$ for individual replicates in the PLL experiment. All parameter estimates are given to two significant figures. The red column in each replicate indicates the level set which gives the minimum least-squares measure.

PLL		Level set ϵ (% of K)					
		1	5	10	15	20	25
Replicate 1	$\bar{D}^{(1)}$ [$\mu\text{m}^2/\text{h}$]	240	380	520	660	800	880
	$\bar{\lambda}^{(1)}$ [/h]	0.12	0.093	0.080	0.072	0.066	0.064
	$E^{(1)}$ ($\times 10^{-2}$)	18	9.2	4.8	2.5	1.3	1.3
Replicate 2	$\bar{D}^{(2)}$ [$\mu\text{m}^2/\text{h}$]	450	760	1100	1500	2000	2200
	$\bar{\lambda}^{(2)}$ [/h]	0.078	0.061	0.052	0.046	0.042	0.043
	$E^{(2)}$ ($\times 10^{-2}$)	22	11	5.2	2.9	3.1	6
Replicate 3	$\bar{D}^{(3)}$ [$\mu\text{m}^2/\text{h}$]	250	440	630	840	1000	1100
	$\bar{\lambda}^{(3)}$ [/h]	0.11	0.086	0.074	0.066	0.061	0.062
	$E^{(3)}$ ($\times 10^{-2}$)	12	4.9	1.8	0.43	0.66	2.6

3 Experimental data describing the carrying capacity density, the initial cell density, and the initial gap width

In this section, we discuss the measure of carrying capacity density, K , and initial cell density, $\mathcal{C}_0^{(r)}$, for the experimental replicates. Our experimental results suggest that regions far behind the edges of the gap are fully occupied by cells after 48 h. Therefore, we directly count the number of cells at $t = 48$ h in the four identical $300 \mu\text{m} \times 150 \mu\text{m}$ rectangular boxes, located $50 \mu\text{m}$ away from the edges of the experimental field-of-view (Figure S2). By averaging the number of cells over the four boxes in each replicate and then further averaging across the individual replicates, we obtain estimates of K listed in Table S4.

To estimate $\mathcal{C}_0^{(r)}$ we count and average the number of cells in the same four identically-sized rectangular boxes for replicate r at $t = 0$ h. In Table S5 we show the estimates of $\tilde{\mathcal{C}}_0$ for the control, gelatin, and PLL experiments, obtained by averaging $\mathcal{C}_0^{(r)}$ across the individual replicates in each experiment.

In addition, in Table S6 we show the data of the average initial gap width, $\tilde{W}(0)$, estimated using the edge detection method (Jin et al. 2018).

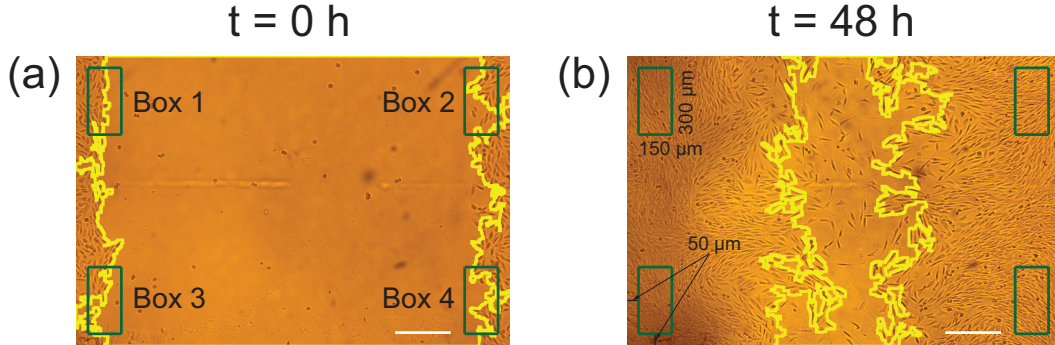


Fig. S2. **Examples of experimental images at $t = 0$ and 48 h.** The green rectangular boxes indicate regions where cell number is counted. The yellow lines indicate the gap edges. The scale bar corresponds to $500 \mu\text{m}$.

Table S4

Estimates of K obtained by measuring and averaging cell numbers in the four identically-sized boxes in experimental images at $t = 48$ h. All estimates are rounded to two decimal places.

K [cells/ μm^2]		Average from replicates	Standard deviation
Control		2.46×10^{-3}	3.88×10^{-4}
Gelatin	Upper	2.48×10^{-3}	8.94×10^{-5}
	Lower	2.34×10^{-3}	6.58×10^{-5}
PLL	Upper	2.41×10^{-3}	8.14×10^{-5}
	Lower	2.45×10^{-3}	7.59×10^{-5}
Average from experiments		2.43×10^{-3}	3.60×10^{-4}

Table S5

Estimates of \tilde{C}_0 obtained by measuring and averaging cell numbers in the four identically-sized boxes in experimental images at $t = 0$ h. All estimates are rounded to two decimal places.

\tilde{C}_0 [cells/ μm^2]		Average from replicates	Standard deviation
Gelatin	Control	1.00×10^{-3}	4.15×10^{-4}
	Upper	9.81×10^{-4}	3.51×10^{-4}
	Lower	1.03×10^{-3}	2.99×10^{-4}
PLL	Upper	9.39×10^{-4}	3.02×10^{-4}
	Lower	1.18×10^{-3}	5.35×10^{-4}
Average from experiments		1.02×10^{-3}	3.91×10^{-4}

Table S6
Estimates of $\widetilde{W}(0)$ measured from experimental images at $t = 0$ h. All estimates are rounded to the nearest integer.

$\widetilde{W}(0)$ [μm]		Average from replicates	Standard deviation
Gelatin	Control	1809	57
	Upper	1678	90
	Lower	1753	90
PLL	Upper	1785	17
	Lower	1726	87
Average from experiments		1750	51

4 Experimental data for individual replicates

Table S7 - Table S9 list the data of $W^{(r)}(t)$ and $N^{(r)}(t)$ for the three replicates in the control experiment. Table S10 - Table S12 list the data of $W^{(r)}(t)$ and $N^{(r)}(t)$ for the three replicates in the gelatin experiment. Table S13 - Table S15 list the data of $W^{(r)}(t)$ and $N^{(r)}(t)$ for the three replicates in the PLL experiment. Table S16 shows the data of $\mathcal{C}_0^{(r)}$ and $K^{(r)}$ measured from individual replicates.

Table S7

Experimental data of $W^{(1)}(t)$ and $N^{(1)}(t)$ for replicate 1 in the control experiment.

Control 1	$W^{(1)}(t)$ [μm]		$N^{(1)}(t)$ [cells]			
t [h]	Upper	Lower	Upper		Lower	
			$N_1^{(1)}(t)$	$N_2^{(1)}(t)$	$N_1^{(1)}(t)$	$N_2^{(1)}(t)$
0	1838	1816	5	3	5	4
12	1686	1680	2	1	3	7
24	1567	1498	12	24	15	33
36	1201	1195	104	62	103	116
48	830	841	164	155	217	137

Table S8
Experimental data of $W^{(2)}(t)$ and $N^{(2)}(t)$ for replicate 2 in the control experiment.

Control 2	$W^{(2)}(t)$ [μm]		$N^{(2)}(t)$ [cells]			
t [h]	Upper	Lower	Upper		Lower	
			$N_1^{(2)}(t)$	$N_2^{(2)}(t)$	$N_1^{(2)}(t)$	$N_2^{(2)}(t)$
0	1745	1737	0	0	2	3
12	1589	1534	9	7	7	9
24	1467	1427	23	35	21	47
36	1279	1290	76	63	76	89
48	996	983	113	153	120	185

Table S9

Experimental data of $W^{(3)}(t)$ and $N^{(3)}(t)$ for replicate 3 in the control experiment.

Control 3	$W^{(3)}(t)$ [μm]		$N^{(3)}(t)$ [cells]			
t [h]	Upper	Lower	Upper		Lower	
			$N_1^{(3)}(t)$	$N_2^{(3)}(t)$	$N_1^{(3)}(t)$	$N_2^{(3)}(t)$
0	1882	1835	4	0	0	0
12	1695	1639	0	1	3	0
24	1504	1485	20	9	14	32
36	1325	1186	22	120	129	61
48	1036	873	132	112	178	148

Table S10

Experimental data of $W^{(1)}(t)$ and $N^{(1)}(t)$ for replicate 1 in the gelatin experiment.

Gelatin 1	$W^{(1)}(t)$ [μm]		$N^{(1)}(t)$ [cells]			
t [h]	Upper	Lower	Upper		Lower	
			$N_1^{(1)}(t)$	$N_2^{(1)}(t)$	$N_1^{(1)}(t)$	$N_2^{(1)}(t)$
0	1753	1856	6	1	13	4
12	1421	1632	23	13	2	0
24	1185	1496	80	72	30	22
36	883	1264	179	182	73	94
48	388	971	270	264	181	147

Table S11

Experimental data of $W^{(2)}(t)$ and $N^{(2)}(t)$ for replicate 2 in the gelatin experiment.

Gelatin 2	$W^{(2)}(t)$ [μm]		$N^{(2)}(t)$ [cells]			
t [h]	Upper	Lower	Upper		Lower	
			$N_1^{(2)}(t)$	$N_2^{(2)}(t)$	$N_1^{(2)}(t)$	$N_2^{(2)}(t)$
0	1704	1711	6	0	1	3
12	1476	1639	10	14	0	3
24	1227	1383	103	59	52	35
36	713	923	151	151	80	158
48	461	761	255	268	156	180

Table S12

Experimental data of $W^{(3)}(t)$ and $N^{(3)}(t)$ for replicate 3 in the gelatin experiment.

Gelatin 3	$W^{(3)}(t)$ [μm]		$N^{(3)}(t)$ [cells]			
t [h]	Upper	Lower	Upper		Lower	
			$N_1^{(3)}(t)$	$N_2^{(3)}(t)$	$N_1^{(3)}(t)$	$N_2^{(3)}(t)$
0	1578	1691	4	2	0	0
12	1365	1534	38	28	1	7
24	1101	1444	68	82	13	50
36	823	1157	151	133	53	94
48	409	1052	174	189	160	112

Table S13

Experimental data of $W^{(1)}(t)$ and $N^{(1)}(t)$ for replicate 1 in the PLL experiment.

PLL 1	$W^{(1)}(t)$ [μm]		$N^{(1)}(t)$ [cells]			
t [h]	Upper	Lower	Upper		Lower	
			$N_1^{(1)}(t)$	$N_2^{(1)}(t)$	$N_1^{(1)}(t)$	$N_2^{(1)}(t)$
0	1800	1753	6	0	9	7
12	1653	1729	7	3	9	0
24	1429	1556	52	30	9	20
36	1153	1304	113	165	57	84
48	879	1035	190	213	163	90

Table S14

Experimental data of $W^{(2)}(t)$ and $N^{(2)}(t)$ for replicate 2 in the PLL experiment.

PLL 2	$W^{(2)}(t)$ [μm]		$N^{(2)}(t)$ [cells]			
t [h]	Upper	Lower	Upper		Lower	
			$N_1^{(2)}(t)$	$N_2^{(2)}(t)$	$N_1^{(2)}(t)$	$N_2^{(2)}(t)$
0	1767	1629	3	2	0	0
12	1495	1615	9	15	7	3
24	1274	1461	91	61	32	25
36	1034	1200	155	140	98	51
48	546	941	198	157	153	135

Table S15

Experimental data of $W^{(3)}(t)$ and $N^{(3)}(t)$ for replicate 3 in the PLL experiment.

PLL 3	$W^{(3)}(t)$ [μm]		$N^{(3)}(t)$ [cells]			
t [h]	Upper	Lower	Upper		Lower	
			$N_1^{(3)}(t)$	$N_2^{(3)}(t)$	$N_1^{(3)}(t)$	$N_2^{(3)}(t)$
0	1786	1796	0	1	0	1
12	1624	1693	17	1	1	1
24	1421	1478	42	41	28	61
36	1101	1153	129	101	113	82
48	727	791	150	235	154	153

Table S16

Experimental data of $C_0^{(r)}$ and K for individual replicates in the three groups. All the data are given to two decimal places.

t [h]	$C_0^{(r)} [\times 10^{-3} \text{ cells}/\mu\text{m}^2]$								$K^{(r)} [\times 10^{-3} \text{ cells}/\mu\text{m}^2]$							
	Upper				Lower				Upper				Lower			
	Box 1	Box 2	Box 3	Box 4	Box 1	Box 2	Box 3	Box 4	Box 1	Box 2	Box 3	Box 4	Box 1	Box 2	Box 3	Box 4
Control 1	1.47	1.10	0.73	0.30	0.97	1.10	0.90	0.93	2.09	2.18	2.31	2.38	1.98	1.60	3.00	2.73
Control 2	1.50	1.03	1.70	1.10	1.53	0.43	1.23	1.43	2.40	2.04	2.20	2.18	2.38	2.47	2.33	2.29
Control 3	0.43	1.57	0.40	1.20	1.10	0.83	0.73	0.37	3.51	2.16	2.44	2.53	2.89	2.73	2.76	2.40
Gelatin 1	1.47	0.83	0.77	0.97	0.73	0.70	1.00	1.03	2.76	2.58	2.53	2.76	2.58	2.60	2.38	2.31
Gelatin 2	1.33	0.83	0.63	0.63	0.87	1.13	0.80	0.80	3.18	2.38	2.96	3.04	2.00	2.31	2.20	2.60
Gelatin 3	1.70	1.10	0.87	0.63	1.47	1.70	1.10	1.07	1.82	1.64	2.47	1.64	2.42	2.09	2.60	2.04
PLL 1	1.10	0.93	1.47	0.60	0.80	1.03	1.17	0.63	2.38	2.27	2.49	2.36	2.62	2.44	2.71	1.84
PLL 2	1.43	0.83	1.07	0.87	2.07	1.87	1.93	1.47	2.07	2.07	2.84	1.98	2.09	2.07	2.16	2.11
PLL 3	1.03	0.60	0.53	0.80	1.07	0.80	0.73	0.53	2.60	2.82	1.89	3.20	2.80	2.71	2.42	1.84

References

- [1] Jin W, Lo KY, Chou SE, McCue SW, Simpson MJ, 2018b. The role of initial geometry in experimental models of wound closing. *Chem Eng Sci.* 179, 221-226.
- [2] Morton KW, Mayers DF, 2005. Numerical Solution of Partial Differential Equations. Cambridge University Press, Cambridge.